A study of film thickness and hydrodynamic entrance length in liquid laminar film flow along a vertical tube

Hongxia Gao[a], Xiao Luo[a]*, Ding Cui, Xiayi Hu[b], Ardi Hartono[c], Hallvard F. Svendsen[c], Zhiwu Liang[a]*

[a]Joint International Center for CO_2 Capture and Storage (iCCS), Provincial Key Laboratory for Cost-effective Utilization of Fossil Fuel Aimed at Reducing Carbon-dioxide Emissions, College of Chemistry and Chemical Engineering, Hunan University, Changsha 410082, China

[b]College of Chemical Engineering, Xiangtan University, Hunan, 411105, China

[c]Department of Chemical Engineering, Norwegian University of Science and Technology, Sem Sælands vei 4, N-7491 Trondheim, Norway

*CORRESPONDING AUTHOR:

Tel: +86-18627329998; fax: +86-731-88573033; E-mail address: x_luo@hnu.edu.cn (X. Luo).

Tel: +86-13618481627; fax: +86-731-88573033; E-mail address: zwliang@hnu.edu.cn (Z. Liang).

Abstract

The liquid film thickness and hydrodynamic entrance length in a vertical tube was studied experimentally and numerically. Measurements using distilled water, 30 wt% MEA and 40 wt% sugar solutions were carried out to investigate the effects of liquid flow rate on the formation of the liquid film. The experimental results validate the new Navier-Stokes based equation in cylindrical coordinates (Eq.16) and the volume of fluid (VOF) model giving a competitively high prediction of the liquid film thickness especially in the low Reynolds number region. In addition, a new empirical model and an improved minimal surface model have been firstly proposed for calculation of the hydrodynamic entrance length, with a relatively reasonable average absolute relative deviation (AARD) of 3.03% and 6.83%, respectively. Furthermore, the effects of the hydrodynamic entry length on the gas-liquid interfacial area calculated by the improved minimal surface model were comprehensively studied, and can be ignored if the ratio of the liquid film length (y) and the hydrodynamic entrance length (λ_E) is lower than 10. However, it should be noted that the hydrodynamic entrance length cannot be ignored in packed columns in which the liquid flow is very complex due to the packings with different structures and materials.

Keywords: Vertical tube; Film thickness; Hydrodynamic entrance length; Falling film.

1 Introduction

Liquid film flow, which has been widely applied for gas-liquid contactors such as tray towers and packed columns, has attracted much attention since the last century. Liquid film thickness is one of the key parameters which has high energy and mass transfer potential due respectively to its high latent heat and mass transfer area. Therefore, it is essential to understand the mechanism of liquid film flow along a vertical tube.

Theoretically, the fluid flow along the vertical tube can be divided into three parts: the entrance flow region, the fully developed flow region, and the uniform flow region (downstream of the asymptotic limit). The entrance flow region, including both the thermal and hydrodynamic entrance regions, is vitally important for heat and mass transfer in a gas-liquid contactor, especially for lab scale apparatus[1]. In addition, it can increase the pressure drag and create skin friction drag which affects the characteristics of the flow. It is reported that the length of the entrance flow region is one of the important factors used to accurately predict the liquid velocity profiles, boundary layer expanding, and gas-liquid contact area. This length is termed as the hydrodynamic entrance length, which can be seen as the intersection point where the film thickness is equal to the boundary layer thickness. Equally, researchers have focused on studies of this developing region of the liquid film since last century. The dimensionless hydrodynamic entrance length of a liquid film has been firstly studied based on different assumed liquid velocity profiles. Andersson et al.[2] proposed a semi-parabolic velocity profile to describe a dilatant fluid, as well as a sinusoidal velocity profile and a third-order polynomial approach to describe a Newtonian fluid. Ruschak et al.[3] and Tekić[4] calculated the dimensionless hydrodynamic entrance length of a falling liquid film based on a semi-parabolic velocity profile. Roy et al. [5] also calculated the dimensionless hydrodynamic entrance length based on a third-degree polynomial velocity profile which was solved by a Runge-Kutta method to determine the boundary layer thicknesses. Then, the dimensionless hydrodynamic entrance length of a laminar thin-film flow along a vertical plate was determined based on a fourth-degree polynomial velocity profile by Schlichting et al.[6]. Trela et al.[7] proposed that the relationship between dimensionless entrance length with the initial film thickness, h_0, in the range of 0.1 to 2 was based on a similar parabolic velocity profile, and indicated that the initial film thickness could be the only parameter that affects the dimensionless entrance length[7]. However, most of the existing empirical or semi-empirical models for dimensionless hydrodynamic entrance length are based on a key parameter $\beta_0=h_0/h_m$ (h_0 and h_m representing the initial film thickness and average film thickness, respectively)[2, 8] without discussing the relationship between the hydrodynamic entrance length and Reynolds number. Furthermore, experiments were done using only a specific fluid (such as water) which might limit their application. In this investigation, the relationship between hydrodynamic entrance length with Reynolds number and surface tension have been studied and discussed to provide better insight to the hydrodynamic entrance length exploration.

Furthermore, film thickness is one of the most important parameters for calculating the hydrodynamic entrance length, as well as a prime and vital parameter governing heat and mass transfer area[9] [10]. Besides, the hydrodynamic behavior of film thickness can also be used to define the transition region between laminar and turbulent flow regimes. Many methods have been used to measure the film thickness of liquid film flow, which could be divided into two main types: direct method and indirect method. Measurements with a micrometer screw or probe are normally taken as direct methods[11]. The measurements by using radioactive tracer[12], electrical capacitance[13] and shadow photographs[14] are the widely used indirect methods.

Many researchers have proposed various models for calculating the film thickness in terms of theory. Nusselt was the first to propose equations for the falling film flow along a vertical tube[15] but these were found to fail to predict the film thickness correctly, even for steady laminar conditions of flow[16]. Kapitsa has proposed a model for predicting the film thickness on a plate[17], but it fails to predict the film thickness for turbulent flow[18]. Then, Bird et al.[19] gave a correlation to calculate the liquid film thickness along a vertical plate[19], and this has become the most commonly used equation. Also, Grigoreva et al.[20], and Grossman et al.[21] have presented a series of equations to calculate the film thickness for flow along a vertical tube. Min et al.[22] made a comparison of those different equations, and found that all of them show inconsistency. Later, Hassan et al.[23] proposed a direct relation between the film thickness and the distance traveled by the liquid flow, while Murty et al.[24] presented an analysis about the flow along an inclined wall that took into consideration the interfacial shear. Although both experimental methods and theories have significantly improved during the past years, there is still little literature about the investigation of liquid film thickness of flow along a cylindrical tube.

In this study, the flow along a cylindrical tube with free surface is firstly investigated experimentally and numerically. The VOF model in CFD software is used to simulate the film flow, because with it, one can obtain both the film thickness and hydrodynamic entrance length[25]. The comparisons between simulation and experimental results are made in order to explore the characteristics of the flow along a cylindrical tube. Finally, both an empirical equation and a minimal surface model are proposed and developed to predict the hydrodynamic entrance length, and the effects on the gas-liquid contact area.

2 Experimental setup and procedures

2.1 Experimental apparatus

In this work, distilled water, 30wt% MEA solution and 40wt% sugar solution were used as working fluids, and their physical properties of density, viscosity and surface tension are presented in Table 1. A vertical cylinder contactor made of polished stainless steel with outer diameter of 10 mm and total exposed length of 75 mm was used for the experimental tests, as shown in Figure 1. The contactor is placed horizontally in an open environment and operated with liquid flow entering at the top, passing through a liquid distributor inside the apparatus and flowing to the bottom along the stainless steel vertical cylinder with its free surface in stationary air. Additionally, a high speed camera with a frame rate of 10000fps, shutter of 1/142000s, resolution of 256 × 256px, and calibration of 8.3±0.1μm/px was used to take the frames of liquid film. A sequence of frames was obtained in five different positions from the vertical cylinder contactor along the liquid flow. The schematic diagram of the experimental setup for hydraulic experiment is presented in Figure 2.

Table 1.

Figure 1.

Figure 2.

2.2 Experimental producer

In order to have good and reproducible laminar flow along the vertical cylinder contactor, a set of hydraulic experiments were performed at 298.15K and ambient pressure to obtain the limits for the laminar flow region, wavy surface region, and the turbulent region. Figure 2 shows the diagram of hydraulic experiments by using the shadow-photographs method, which involves a high speed camera to test the hydraulic phenomena in different systems. The shadow pictures obtained from the high speed camera show the liquid film phenomena, which includes the variations in the liquid film thickness as a function of liquid flow rate, as illustrated in Figure 3.

Figure 3.

As shown in Figure 3a, which is the laminar flow at the top of the cylinder near the entrance at a very low liquid flow rate, the hydrodynamic entrance effect obviously does exist. However, the hydrodynamic entry length only takes no more than 5% of the whole exposed length and can be considered to be negligible. Figure 3b shows the laminar flow in the other parts of the cylinder from which the film thickness of the laminar flow can be accurately acquired. However, a rippling behavior occurs as the Reynolds number increased as shown in Figure 3c. It is important to avoid the waving effects when the film flow is being studied at the gas liquid absorption interface since it greatly influences the contact area, and makes the film thickness to become nonuniform. Consequently, the waving behavior of the liquid film was avoided in this study, and the Reynolds number which causes the rippling of the liquid film is seen as a critical point between the laminar flow region and the transition region.

The width, measured as pixel points of liquid film shadows at various liquid flow rates can be obtained when the distance between the cylinder and high speed camera is fixed. The diameter of the stainless steel cylinder is known as d_0 and its pixel point pp_0, can be obtained by using an Image Software. Then, the film thickness can be easily calculated using Eq. 1:

$$\delta = \frac{d_0}{pp_0} \cdot pp - d_0 \tag{1}$$

When the uniform flow enters the vertical cylinder contactor, a boundary layer begins to develop along the pipe due to the effect of the viscosity of solution. The hydrodynamic entrance length is defined as a distance, that a flow travels after entering a pipe for internal flow before the flow becomes fully developed, as shown in Figure 4a; or a gap for external flow before the film thickness has reached its asymptotic value within a deviation of 1% [26, 27], as shown in Figure 4b.

Figure 4.

3 Models and simulation

3.1 CFD model

CFD (computational fluid dynamics) is usually used to solve thin fluid film problems as it can overcome the limitations of the classical Reynolds equation and evaluate the data quickly. CFD has become more capable of readily modeling fluid flow as computational ability has rapidly increased and become able to offer the potential of fine-mesh and detailed simulations. In this investigation, the model of the liquid film flow along the vertical tube was developed by Fluent 6.3 and the 2D model was designed by Gambit software. The fluent solvers are based on the finite volume method in which the domain is discretized into a finite set of control volumes or cells, and the general conservation (transport) equations for mass, momentum, energy and so on are discretized into algebraic equations.

3.1.1 Grid generations and validation

In general, quad/hex meshes are normally selected to create simple geometries as they can provide higher-quality solutions with fewer cells than a comparable tri/tet meshes. In the present work, the quad mesh was selected to create a 2D model. In addition, numerous grids with varying fineness of mesh were created for grid independence testing. The film thickness and hydrodynamic entrance length of water with different number of grids for which the flow rate was set to be 54.25 mL/min were compared as shown in Table 2. It can be concluded that the simulation results can be seen to be independent of the number of grids. However, it costs more time but results in poorer accuracy for computations with a very large number of grids. Therefore, 635110 was chosen as the mesh number in this case.

Table 2.

3.1.2 Simulation set-up

3.1.2.1 Solver set-up

In general, the model of a low-speed incompressible flow selects the pressure-based approach as the numerical method in which the pressure field is extracted by solving pressure correction equations obtained by manipulating continuity and momentum equations. The velocities are obtained from the momentum and continuity equations.

3.1.2.2 Multiphase model selection

Regarding the simulation of a two-phase flow along the vertical tubes with free surface, VOF (volume of fluid) has been verified to be a suitable model since it can simulate two or more immiscible fluids by solving a single set of momentum equations and tracking the volume fraction of each of the fluids throughout the domain. One of its typical applications is to predict steady or transient tracking of any liquid-gas interface[22].

3.1.2.3 Viscous model selection

The laminar flow model was selected in this study due to the low Reynolds number and the fact that the fluid flow is in the laminar region. Mass and momentum conservation equations were solved, as described in Eqs. 2 and 3, respectively.

$$\frac{\partial \rho}{\partial t}+\frac{\partial}{\partial x_i}\left(\rho u_i\right)=S_m \tag{2}$$

$$\frac{\partial}{\partial t}\left(\rho u_i\right)+\frac{\partial}{\partial x_j}\left(\rho u_i u_j\right)=-\frac{\partial P}{\partial x_i}+\frac{\partial \tau_{ij}}{\partial x_j}+\rho g_i+F_i \tag{3}$$

The stress tensor can be calculated by Eq. 4

$$\tau_{ij}=\left[\mu\left(\frac{\partial u_i}{\partial x_j}+\frac{\partial u_j}{\partial x_i}\right)\right]-\frac{2}{3}\mu\frac{\partial u_i}{\partial x_i}\delta_{ij} \tag{4}$$

3.1.2.4 Boundary conditions and solutions controls

Velocity at the inlet and outlet flow were set in order to be suitable for the incompressible fluid in this case. PISO algorithm (Pressure Implicit with Splitting of

Operator) was selected as the numerical method pressure-velocity coupling for its wide use for unsteady flow problems. Second-order upwind scheme was chosen as the discretization method due to using larger ‘stencil’ for 2nd order accuracy. The various CFD settings are summarized in Table 3 below:

Table 3.

3.2 Model of film thickness

Considering the flow of a fluid along a flat surface (as shown in Figure 5 (a)), Bird et al.[19] reported a correlation (Eq. 5) to calculate the liquid film thickness along a vertical wall. Since there is no model given for the film flow along a cylinder, as shown in Figure 5 (b), it has been assumed that the width of the plate is equal to the circumference of the vertical cylinder. This enables the prediction of the liquid film thickness along the vertical cylinder. The present work proposes a formula (Eq. 15 and Eq. 16) based on cylindrical coordinates which gives a more reasonable calculation.

Figure 5.

$$\delta = \sqrt[3]{\frac{3\mu Q}{\rho g W}} = \sqrt[3]{\frac{3\mu Q}{2\rho g \pi R}} \tag{5}$$

According to the Navier-Stokes equation, the equation of motion for laminar flow along a cylinder as shown in Figure 5 (b) can be simplified as:

$$\mu \frac{1}{r}\frac{d}{dr}\left(r\frac{du}{dr}\right) = -\rho g \tag{6}$$

The general solution to Eq. 6 can easily be obtained as:

$$\mu \frac{du}{dr} = -\frac{1}{2}\rho g r + \frac{c}{r} \tag{7}$$

and

$$u=\frac{1}{4}\frac{\rho g}{\mu}\left(R^2-r^2\right)+\frac{c}{\mu}ln\left(\frac{r}{R}\right) \tag{8}$$

Here the no-slip boundary condition $u|_{r=R}=0$ has been used. From Eq. 7 and Newton's law, the shear stress can be expressed as:

$$\tau_w=-\frac{1}{2}\rho gR+\frac{c}{R} \tag{9}$$

On the other hand, from force balance, we have

$$\tau_w\left(2\pi RH\right)=\rho g\pi\left[\left(R+\delta\right)^2-R^2\right]H \tag{10}$$

Then

$$R\tau_w=\frac{1}{2}\rho g\left(2R\delta+\delta^2\right) \tag{11}$$

From Eq. 8 and 10:

$$c=\frac{1}{2}\rho g\left(R+\delta\right)^2 \tag{12}$$

Hence,

$$\begin{aligned} u&=\frac{\rho g}{4\mu}\left(R^2-r^2\right)+\frac{\rho g}{2\mu}\left(R+\delta\right)^2 ln\left(\frac{r}{R}\right) \\ &=\frac{\rho gR^2}{4\mu}\left[2\left(1+\alpha\right)^2 ln\left(\varphi\right)+1-\varphi^2\right] \end{aligned} \tag{13}$$

Where $\varphi=r/R$ and $\alpha=\delta/R$. Thus,

$$\begin{aligned} Q&=2\pi\int_R^{R+\delta} rudr=\frac{\pi\rho gR^4}{2\mu}\int_1^{1+\alpha}\varphi\left[2\left(1+\alpha\right)^2 ln\left(\varphi\right)+1-\varphi^2\right]d\varphi \\ &=\frac{\pi\rho gR^4}{8\mu}\left[4\left(1+\alpha\right)^4 ln\left(1+\alpha\right)-\alpha\left(2+\alpha\right)\left(2+6\alpha+3\alpha^2\right)\right] \end{aligned} \tag{14}$$

These can be rewritten as:

$$\frac{3\mu Q}{\rho g(2\pi R)}=\frac{3R^3}{16}\left[4(1+\alpha)^4\ln(1+\alpha)-\alpha(2+\alpha)(2+6\alpha+3\alpha^2)\right] \tag{15}$$

and

$$\frac{3\mu\bar{u}}{\rho g R^2} = \frac{3}{8}\left[4\frac{(1+\alpha)^4\ln(1+\alpha)}{(2+\alpha)\alpha} - \left(2+6\alpha+3\alpha^2\right)\right] \tag{16}$$

The correlation of Bird et al. for liquid film on flat plate can be transformed from Eq. 5 as

$$\frac{3\mu Q}{\rho g W} = \frac{3\mu Q}{\rho g(2\pi R)} = \delta^3 = R^3\alpha^3 \tag{17}$$

or

$$\frac{3\mu\bar{u}}{\rho g} = \delta^2 = R^2\alpha^2 \tag{18}$$

4 Results and Discussion

The film thickness and hydrodynamic entrance length were obtained experimentally, as tabulated in Tables 4-6. All the experimental results of film thickness and hydrodynamic entrance length were used to determine if the entrance length effect should be neglected. As presented in the tables 4-6, it can be observed that the hydrodynamic entry length only takes less than 8.22% of the whole length (75mm) of the cylinder. Therefore, it can be concluded that the hydrodynamic entry length effect is negligible when calculating the whole contact surface area, especially for differential reactors. However, in the case of very fast reactions, the heat and mass transfer will take place at very short range close to the entrance; in which case, the hydrodynamic entry length effect should be taken into account. In addition, the experimental data obtained under different materials and liquid flow rates were used to assess the results of simulation/modeling.

Table 4.

Table 5.

Table 6.

4.1 Liquid film thickness

In order to avoid the impact of entrance effect, only 60 mm of the total cylinder length (75mm) from the bottom was taken into consideration to calculate the average film thickness. For the experiments, the liquid film thicknesses for different liquid flow rates were measured by using Image Software. Figure 6 presents a comparison of the film thickness calculated by Bird et al. equation and the model (Eq.16) proposed in this work. It can be seen from Figure 6 that there is a significant difference between the two calculations at the high liquid flow rate region. On the other hand, the deviation in the range of low liquid flow rates is insignificant. Since experimental liquid flow rates are in the range of 0-200 mL/min, it can be seen that there is no significant difference between the two methods, as shown in Figure 6. Consequently, both Bird's equation and Eq. 16 can be used in this calculation. However, for those cases for which the liquid flow rate is large enough, the model developed from cylindrical liquid film flow based on the cylindrical coordinates (Eq. 16) might be suitable than Bird's equation which is based on the flat plate liquid flow in this case, due to the experiments in this work were carried out in a cylindrical setup.

Figure 6.

The comparisons of experimental liquid film thickness for three systems and the thickness calculated using Bird's equation, Eq. 16 and CFD simulations are illustrated in Figure 7. It can be seen that there is no significant difference among the experimental liquid film thickness and values calculated by Bird's equation and Eq.16 proposed in this work, as well as the CFD simulation results. This demonstrates that both proposed

Eq.16 and CFD model can be used to accurately predict the liquid film thickness at low Reynolds number under the experimental conditions for different liquid systems.

Figure 7.

4.2 Hydrodynamic entrance length

It can be seen from Figure 8 that the hydrodynamic entrance length using water, MEA, and sugar solution (40 wt%) increased as the flow rate increased for both simulation results and the experiment data. This phenomenon indicates that the hydrodynamic entrance length is influenced by the flow rate, or Reynolds number. It can also be clearly seen that there are significant differences between experimental results and simulation, and the hydrodynamic entrance lengths obtained from the simulation are always larger than the experimental results. The main reason is that the roughness in the experimental setup is neglected in simulation whereas it has been verified that the boundary layer thickness will increase as the roughness decreases[28, 29]. Besides, the wall shear stress is also neglected in the simulation whereas it has also been verified that the boundary layer thickness will increase as the wall shear stress is increased[3]. The hydrodynamic entrance length will decrease as the boundary layer length increases according to the literature[6]. Therefore, it implies that the hydrodynamic entrance length acquired from the simulation will be larger than in the real case. Thus, it can be concluded that the CFD simulation using VOF model is not able to adequately simulate the hydrodynamic entry length properly, implying that a better numerical model is required.

Figure 8.

4.2.1 Empirical equation

It is well known that many investigations regarding empirical models for predicting the hydrodynamic entry length exist. However, the models, so far, are still very complicated and have low prediction ability. The dimensionless hydrodynamic entry length (λ) is defined as the ratio between the hydrodynamic entry length (λ_E) and the radius of cylinder (R). Figure 9 shows the variation of the experimental dimensionless hydrodynamic entry lengths with Reynolds number. It can be seen from the figure that for each solution, with different viscosity and surface tension, the hydrodynamic entry length increases with Reynolds number non-linearly. This phenomena can be correlated to the hydrodynamic entry length model obtained in the liquid pipe flow[30, 31]. Therefore, there seems to be a relationship between liquid pipe flow and liquid falling film flow with a free surface. In addition, relationships of the parameters in a linear correlation can be observed as functions of the product of viscosity and surface tension for each liquid system. Therefore, the empirical model of dimensionless hydrodynamic entry length (λ) of falling film flow can be written as:

$$\lambda = a \cdot \mathrm{Re} + b \tag{19}$$

$$a = 0.0008 \cdot e^{8197 \cdot \mu \cdot \sigma} \tag{20}$$

$$b = -1749.3 \cdot \mu \cdot \sigma + 0.8632 \tag{21}$$

here, μ is the liquid viscosity (Pa·s) and σ is the liquid surface tensor (N/m).

Figure 9.

Figure 10 shows comparisons between calculated and experimental hydrodynamic entry length, with an AARD of 3.03%. However, the application of this empirical model is still very limited since the dimensionless hydrodynamic entry length becomes a function of two physical properties instead of dimensionless numbers. Thus, a more theoretically-based model is needed in order to predict the hydrodynamic entry length with fewer and more reasonable parameters.

Figure 10.

4.2.2 Minimal surface model

Figure 11.

As shown in Figure 11b, the shape of the liquid surface near the hydrodynamic entrance is actually a rotating surface formed by generatrix $\kappa(\zeta)$ rotating once on axis ζ. Based on the differential geometric theory, the mean curvature of the rotating surface can be expressed as:

$$2C = \frac{\zeta''}{\left(1+\zeta'^2\right)^{3/2}} + \frac{\zeta'}{\kappa\left(1+\zeta'^2\right)^{1/2}} = \frac{\kappa\zeta'' + \zeta'\left(1+\zeta'^2\right)}{\kappa\left(1+\zeta'^2\right)^{3/2}} \tag{22}$$

Here C is the mean curvature, and the ζ' and ζ'' can be expressed as:

$$\zeta' = \frac{d\zeta}{d\kappa} \qquad \zeta'' = \frac{d^2\zeta}{d\kappa^2} \tag{23}$$

According to Figure 11a,

$$\zeta = \frac{z}{R} \qquad \delta = \frac{r}{R} \qquad \kappa = \frac{R+\delta}{R} \tag{24}$$

When the liquid flow rate is very small, the liquid surface area has a tendency to be minimized due to surface tension effect. When the rotating surface area becomes a minimum, the mean curvature C is now zero; therefore, the equation 25 can be obtained based on Eq.22.

$$\kappa\zeta'' + \zeta'\left(1 + \zeta'^2\right) = 0 \tag{25}$$

Thus, the 1st order derivative of generatrix $\kappa(\zeta)$ can be given as:

$$\zeta' = \pm \frac{\beta}{\sqrt{\kappa^2 - \beta^2}} \tag{26}$$

and

$$\zeta = \beta \ln\left(\frac{\kappa_0 + \sqrt{\kappa_0^2 - \beta^2}}{\kappa + \sqrt{\kappa^2 - \beta^2}}\right) \tag{27}$$

Here, β is the undetermined parameter which relates to the fluid properties and flow state, κ_0 is the dimensionless radial position at the entrance of the cylinder.

Actually, Eq. 27 expresses a suspended chain curve, which shows that κ decreases initially to a minimum value, and then increases after the minimum value with increasing ζ. In this case, this minimum value should be κ_∞ which also equals to the liquid film thickness of steady flow. That means, based on Eq.19, this extreme point should be $\beta = \kappa_\infty$ in order to make $\kappa' = 0$ (or $\zeta' = \infty$). Therefore Eq. 27 can be expressed as

$$\zeta = \kappa_\infty \ln\left(\frac{\kappa_0 + \sqrt{\kappa_0^2 - \kappa_\infty^2}}{\kappa + \sqrt{\kappa^2 - \kappa_\infty^2}}\right) \tag{28}$$

Here, κ_∞ is the dimensionless radial position at the infinite position of the cylinder. Thus, the dimensionless hydrodynamic entrance length can be obtained by:

$$\lambda = \kappa_\infty \ln\left(\frac{\kappa_0 + \sqrt{\kappa_0^2 - \kappa_\infty^2}}{\kappa_\infty}\right) \tag{29}$$

Obviously, the minimal surface model is only suitable for the situation where the liquid flow rate is very small. For the cases of the whole range of liquid flow rates, a correction factor is needed and can be introduced as:

$$\zeta = \gamma \kappa_\infty \ln\left(\frac{\kappa_0 + \sqrt{\kappa_0^2 - \kappa_\infty^2}}{\kappa + \sqrt{\kappa^2 - \kappa_\infty^2}}\right) \tag{30}$$

or

$$\lambda = \gamma \kappa_\infty \ln\left(\frac{\kappa_0 + \sqrt{\kappa_0^2 - \kappa_\infty^2}}{\kappa_\infty}\right) \tag{31}$$

This correction factor, γ, should relate to the fluid properties and flow states. It can be observed from the hydrodynamic experiments that the correction factor is proportional to the ratio of shear stress and gravity as shown in Figure 12, and can be expressed as:

$$\gamma = mX + n \tag{32}$$

Here, m and n are undetermined parameters, and X is the ratio of shear stress and gravity.

$$X = \frac{\mu \bar{v}}{\rho g R^2} \qquad \bar{v} = \frac{Q}{\pi R^2} \;\; or \;\; \frac{Q}{\pi R^2\left(\kappa_0^2 - 1\right)} \tag{33}$$

Figure 12.

It can be found that the parameters m and n for water, 30wt% MEA solution and 40wt% sugar solution are all linear with their Bond number and density, respectively.

$$m = c_1 Bo + c_2 \tag{34}$$

$$n = c_3 \rho + c_4 \tag{35}$$

here

$$Bo = \frac{\sigma}{\rho g R^2} \tag{36}$$

The ratio of shear stress and gravity (X), Bond number (Bo), and the parameters m and n for water, 30wt% MEA solution and 40wt% sugar solution are presented in Tables 7 and 8. In addition, the parity plot in Figure 13 shows that the experimental dimensionless hydrodynamic entry lengths were in good agreement with the predicted values calculated by the developed minimal surface model in this work with AARD of 6.83%, which is in an acceptable range.

Table 7.

Table 8.

Figure 13.

4.3 Gas-liquid interfacial area

In gas absorption process, gas-liquid interfacial area reflects available effective interfacial area for gas and liquid, and thus has a great impact on the mass transfer performance. In general, this gas-liquid interfacial area can be regarded as the cylinder surface area by rotating the liquid film length. In practice, the gas-liquid interfacial area cannot be simplified as the calculated cylindroid area, due to the influence of having different hydrodynamic entrance lengths for different liquid systems. Therefore, the minimal surface model proposed in section 4.2.2 is suitable to accurately calculate the gas-liquid interfacial area in the present work. The relationship between $(A_1-A_2)/A_2$ values and y/λ_E values is given in Figure 13. Here, the A_1 and A_2 are the superficial area with and without consideration of the hydrodynamic entrance length, respectively; y is the liquid film length and λ_E is the hydrodynamic entrance length.

Figure 14.

It can be concluded from Figure 14 that the hydrodynamic entrance length has a significant effect on the gas-liquid interfacial area. The influence of y/λ_E value on the $(A_1-A_2)/A_2$ value can be negligible when the ratio of liquid film length y and hydrodynamic entrance length λ is lower than 20. In contrast, there is a sudden drop in the values of $(A_1\text{-}A_2)/A_2$ with the decrease of y/λ_E values. Thus, the effects of hydrodynamic entrance length must be considered to calculate the gas-liquid interfacial area, which is associated with the mass transfer coefficients of packed columns. In addition, the hydrodynamic entrance length should be considered in gas absorption process when the value of $(A_1\text{-}A_2)/A_2$ is higher than 1% in which the y/λ_E value is below 10. However, it should be noted that the hydrodynamic entrance length cannot be ignored in packed columns in which the liquid flow is very complex due to the packings with different structures and materials.

5 Conclusion

The film thickness of laminar flow has been thoroughly investigated as it is a vital factor of heat and mass transfer processes. The behavior of liquid film falling around a vertical tube was investigated for the determination of liquid film thickness and hydrodynamic entrance length using the shadow-photographs method. Here, three liquids, namely, distilled water, 30wt% aqueous MEA solution and 40wt% sugar solution were used to estimate the effect of liquid flow rate on the formation of liquid film. In addition, a developed Navier-Stokes equation (Eq.16) and the volume of fluid (VOF) model using computational fluid dynamics (CFD) simulation were developed and used to predict the values of experimental film thickness with high predictability, especially in the low Reynolds number region.

However, the comparison between the predicted values and experimental data of the hydrodynamic entrance length indicated that the VOF model is not applicable for prediction of hydrodynamic entrance length. Based on the experimental data, a new empirical model and an improved minimal surface model were developed and used to predict the hydrodynamic entrance length, with AARD of 3.03% and 6.83%, respectively. However, the application of empirical correlations are still quite limited, and the minimal surface model has a little bit less prediction ability but a much larger applicable range.

Furthermore, the gas-liquid interfacial area is an important factor in separation process area. Thus, the effects of the hydrodynamic entry length on the gas-liquid interfacial area were also studied. The calculated values based on the improved minimal surface model showed that the hydrodynamic entry length effect can be neglected in calculating the whole contact surface area if the hydrodynamic entry length only takes less than 8.22% of the whole length. However, in the case of very fast reaction, the heat and mass transfer will take place at a very short range close to entrance; in which case, the hydrodynamic entry length effect should be taken into account.

Acknowledgements

The financial support from the National Natural Science Foundation of China (NSFC-Nos. 21536003, 21776065, 21706057, 1606078, 21406057, 21476064, 21376067 and 51521006), the National Key Technology R&D Program (MOST-No. 2014BAC18B04), the Innovative Research Team Development Plan (MOE-No. IRT1238), the Natural Science Foundation of Hunan Province in China (No. 2016JJ2015), the Guangxi Natural Science Foundation (No. 2016GXNSFAA380190), the China Outstanding Engineer Training Plan for Students of Chemical Engineering & Technology in Hunan University (MOE-No.2011-40), the Opening Project of Guangxi Colleges and Universities Key Laboratory of Beibu Gulf Oil and Natural Gas Resource Effective Utilization (2016KLOG17, 2016KLOG13, 2016KLOG11 and 2016KLOG05), and the China Scholarship Council (CSC) gratefully acknowledged.

NOTATION

Bo	Bond number
C	mean curvature
d_0	diameter of the stainless, m
D	diameter of pipe, m
F_i	extrernal volume force in the direction of i, N
H	Henry's law constant, -
P	static pressure, N
pp	pixel points of the shadow of the stainless steel when the liquid fall flow along the cylinder, -
pp_0	pixel points of stainless steel without liquid flow, -
Q	volumetric flowrate, m^3/h
r	radial position of cylinder, m
R	radius of cylinder, m
Re	Reynolds number, -
S_m	mass which come from dispersed second phase to first phase, kg
u	linear velocity of liquid, m/s
$\overline{u}$	mean velocity of liquid, m/s
V	volume of the cell, m^3
W	circumference of cylinder in wetted wall column, m
X	ratio of shear stress and gravity, -
z	axial position of cylinder, m

Greek letters

γ	correction factor in Eq. 32, -
δ	film thickness, m
δ_0	boundary film thickness, m
$\bar{\delta}$	average film thickness, m
μ	viscosity, kg/m/sec
ρ	density, kg/m^3
τ_w	shear stress, N
λ	dimensionless hydrodynamic entrance length, -
λ_E	hydrodynamic entrance length, mm
κ	dimensionless radial position, -
σ	surface tension, N/m
ζ	dimensionless axial position, -

References

[1] D. Jasikova, M. Kotek, V. Kopecky, An effect of entrance length on development of velocity profile in channel of millimeter dimensions, in: Application of Experimental & Numerical Methods in Fluid Mechanics & Energy: XX Anniversary of International Scientific Conference, 2016, pp. 1154-1160.

[2] H.I. Andersson, T. Ytrehus, Falkner-Skan Solution for Gravity-Driven Film Flow, Journal of Applied Mechanics, 52 (1985) 783-786.

[3] K.J. Ruschak, S.J. Weinstein, Thin-Film Flow at Moderate Reynolds Number, Journal of Fluids Engineering, 122 (2000) 774-778.

[4] M.N. Tekić, D. Pošarac, D. Petrović, Entrance region lengths of laminar falling films, Chemical Engineering Science, 39 (1984) 165-167.

[5] T.R. Roy, On Laminar Thin-Film Flow Along a Vertical Wall, Journal of Applied Mechanics, 51 (1984) 691-692.

[6] P.S. Lawrence, B.N. Rao, Similarity solutions for laminar thin-film flow along a vertical wall, Journal of Physics D: Applied Physics, 26 (1993) 928.

[7] M. Trela, Minimum wetting rate for a decelerating liquid film, International Journal of Heat and Fluid Flow, 9 (1988) 415-420.

[8] H.I. Andersson, Numerical solutions of a TSL-model for free-surface flows, in: Proceedings of Fifth GAMM Conference on Numerical Methods in Fluid Mechanics, Notes on Numerical Fluid Mechanics, Vieweg Verlag, 1984.

[9] M. Masjedi, M.M. Khonsari, On the effect of surface roughness in point-contact EHL: Formulas for film thickness and asperity load, Tribology International, 82 (2015) 228-244.

[10] N. Teichert, A. Auge, E. Yüzüak, I. Dincer, Y. Elerman, B. Krumme, H. Wende, O. Yildirim, K. Potzger, A. Hütten, Influence of film thickness and composition on the martensitic transformation in epitaxial Ni–Mn–Sn thin films, Acta Materialia, 86 (2015) 279-285.

[11] H.C. Kang, M.H. Kim, The development of a flush-wire probe and calibration method for measuring liquid film thickness, International Journal of Multiphase Flow, 18 (1992) 423-437.

[12] M.L. Jackson, Liquid films in viscous flow, AIChE Journal, 1 (1955) 231-240.

[13] V. Nakoryakov, B. Pokusaev, V. Khristoforov, S. Alekseenko, An experimental study of the flow of a liquid film along a vertical wall, Journal of engineering physics, 27 (1974) 1055-1058.

[14] S. Alekseenko, V. Nakoryakov, B. Pokusaev, V. Khristoforov, Friction during downward film flow along a vertical wall, Journal of Engineering Physics, 24 (1973) 584-588.

[15] W. Nusselt, Die Oberflachenkondesation des Wasserdamffes the surface condensation of water, Zetrschr. Ver. Deutch. Ing., 60 (1916) 541-546.

[16] S. Kamei, J. Oishi, Hold-up in wetted wall tower, Mem. Fac. Eng. Kyoto Univ, 18 (1956) 1-12.

[17] P. Kapitza, S. Kapitza, Wave flow of thin viscous fluid layers, Zh. Eksp. Teor. Fiz, 18 (1948).

[18] S. Portalski, Studies of falling liquid film flow Film thickness on a smooth vertical plate, Chemical Engineering Science, 18 (1963) 787-804.

[19] R. Bird, W. Stewart, E. Lightfoot, Transport Phenomena, Wiley, New York, 1960.

[20] V. Nakoryakov, N. Grigor'eva, Combined heat and mass transfer during absorption in drops and films, Journal of Engineering Physics and Thermophysics, 32 (1977) 243-247.

[21] G. Grossman, Simultaneous heat and mass transfer in film absorption under laminar flow, International Journal of Heat and Mass Transfer, 26 (1983) 357-371.

[22] J.K. Min, I.S. Park, Numerical study for laminar wavy motions of liquid film flow on vertical wall, International Journal of Heat and Mass Transfer, 54 (2011) 3256-3266.

[23] N.A. Hassan, Laminar flow along a vertical wall, Journal of Applied Mechanics, 34 (1967) 535-537.

[24] N.S. Murty, V.M.K. Sastri, Accelerating laminar liquid film along an inclined wall, Chemical Engineering Science, 28 (1973) 869-874.

[25] M. Eesa, M. Barigou, CFD simulation of transverse vibration effects on radial temperature profile and thermal entrance length in laminar flow, Aiche Journal, 57 (2015) 51-56.

[26] R.L. Cerro, S. Whitaker, Entrance region flows with a free surface: the falling liquid film, Chemical Engineering Science, 26 (1971) 785-798.

[27] A. Stücheli, M.N. Özişik, Hydrodynamic entrance lengths of laminar falling films, Chemical Engineering Science, 31 (1976) 369-372.

[28] L. Keirsbulck, L. Labraga, A. Mazouz, C. Tournier, Surface roughness effects on turbulent boundary layer structures, Journal of fluids engineering, 124 (2002) 127-135.

[29] S. Srirattayawong, S. Gao, Surface Roughness Effects on Fluid Flow between Two Rotating Cylinders, in: Key Engineering Materials, Trans Tech Publ, 2015, pp. 275-280.

[30] B. Atkinson, M. Brocklebank, C. Card, J. Smith, Low Reynolds number developing flows, AIChE Journal, 15 (1969) 548-553.

[31] F. Durst, S. Ray, B. Ünsal, O. Bayoumi, The development lengths of laminar pipe and channel flows, Journal of fluids engineering, 127 (2005) 1154-1160.

Figures

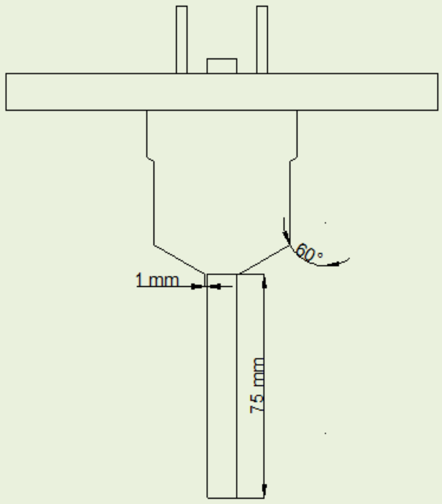

Figure 1. Vertical cylinder contactor.

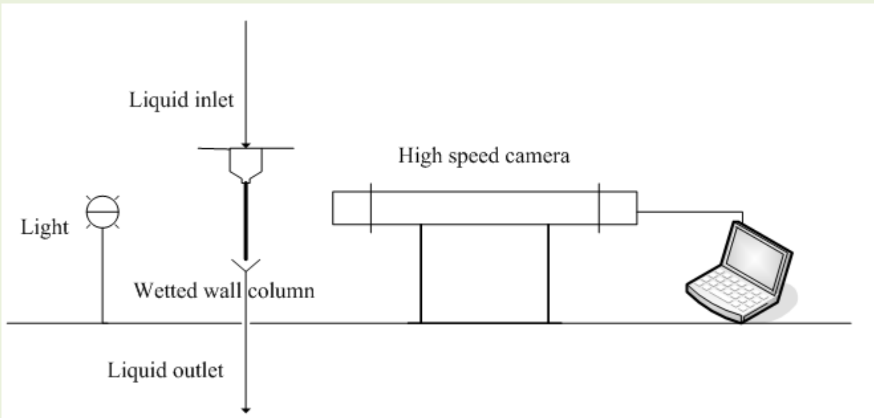

Figure 2. Schematic diagram of the hydraulic experiment setup.

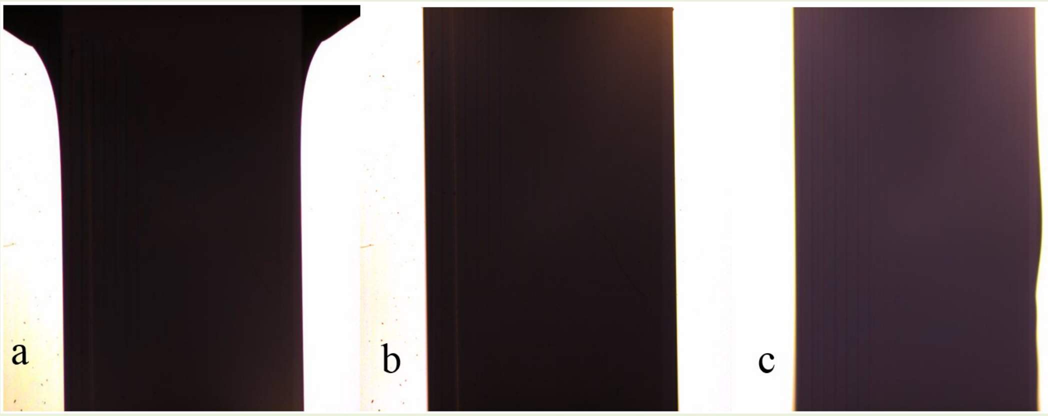

Figure 3. Picture from high speed camera showing film plus steel rod:

a) The position at the entrance; b) the position in the middle of the cylinder; c) the position in the middle of the cylinder with rippling behavior.

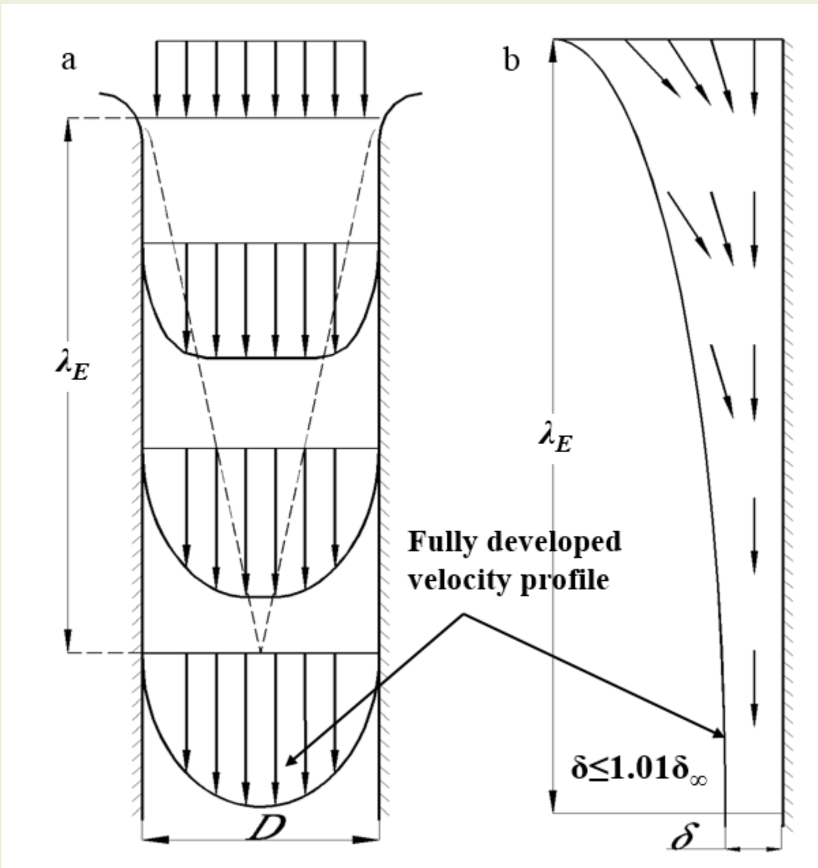

Figure 4. Schematic diagram for the hydrodynamic entrance length in (a) a pipe and (b) a gap.

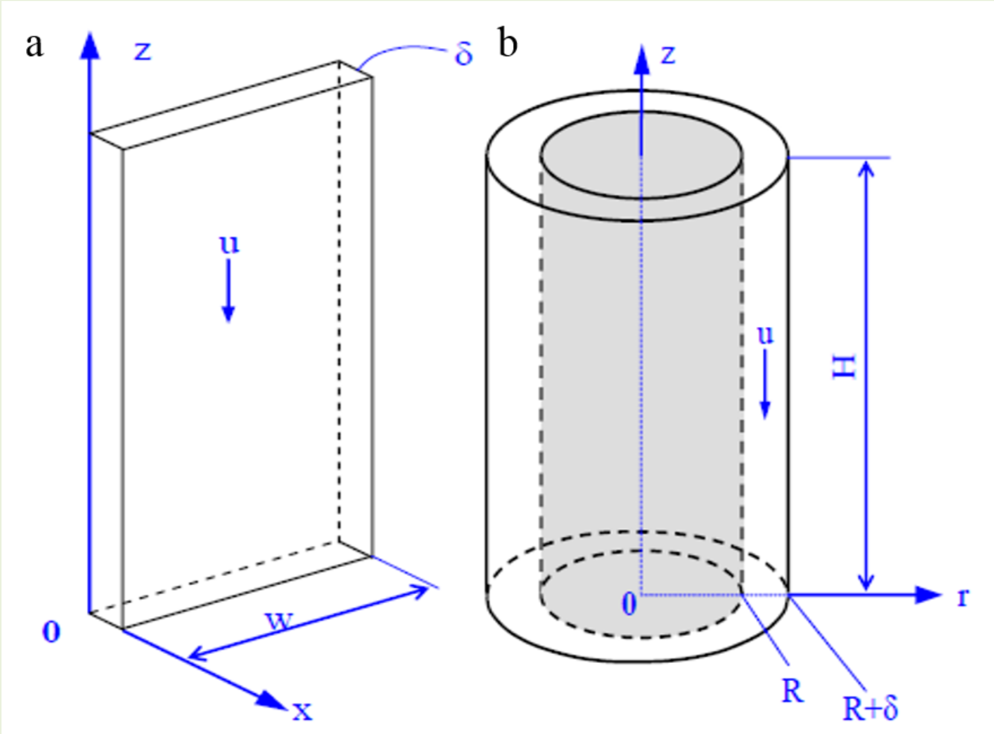

Figure 5. Sketch of a laminar flow along the external surface of (a) a vertical flat plate and (b) a vertical cylinder.

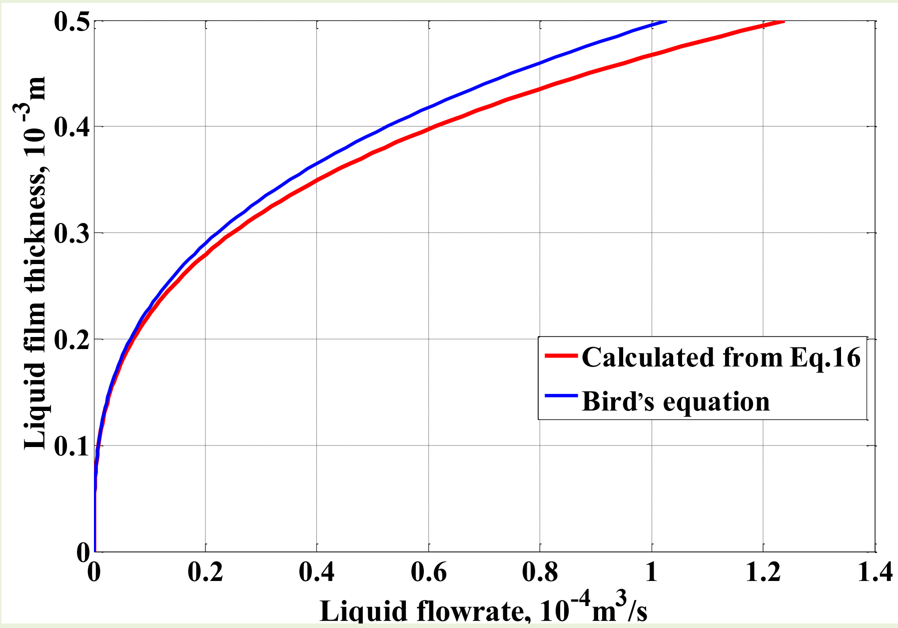

Figure 6. Comparison of calculated film thickness of water between Bird's equation and Eq.16 proposed in this work.

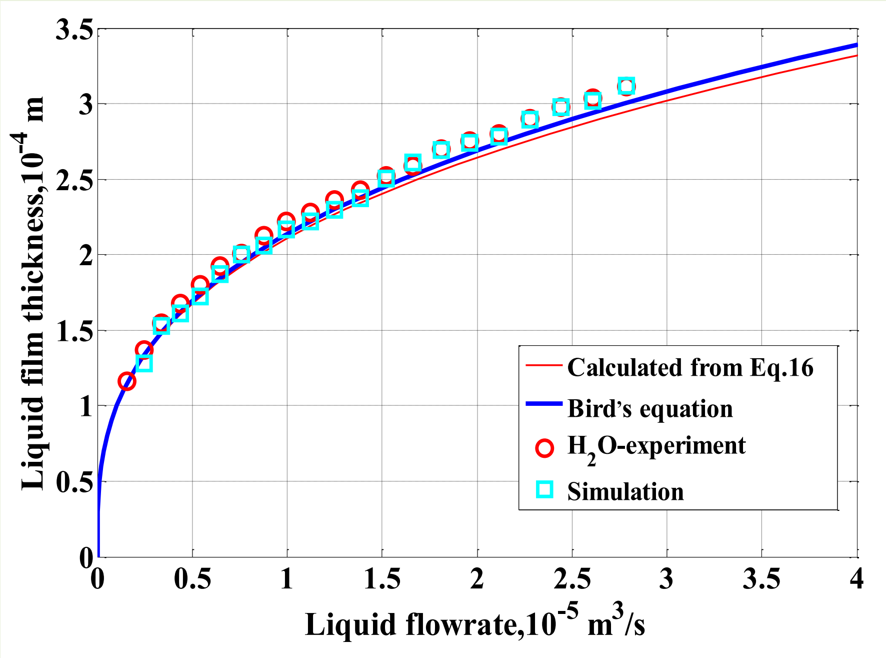

Figure 7a. The liquid film thickness comparison results of H_2O.

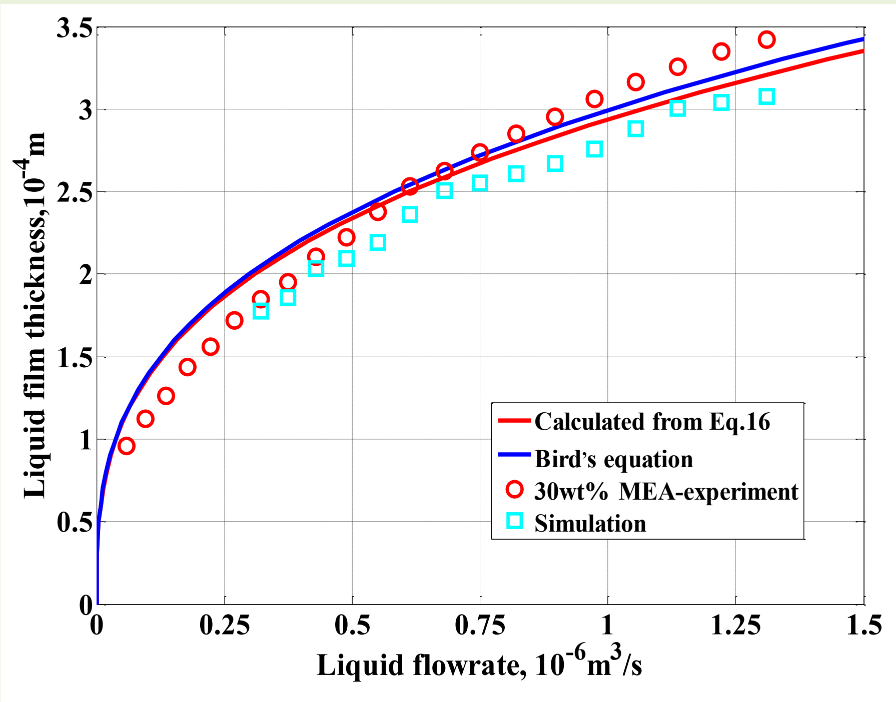

Figure 7b. The liquid film thickness comparison results of 30 wt% MEA.

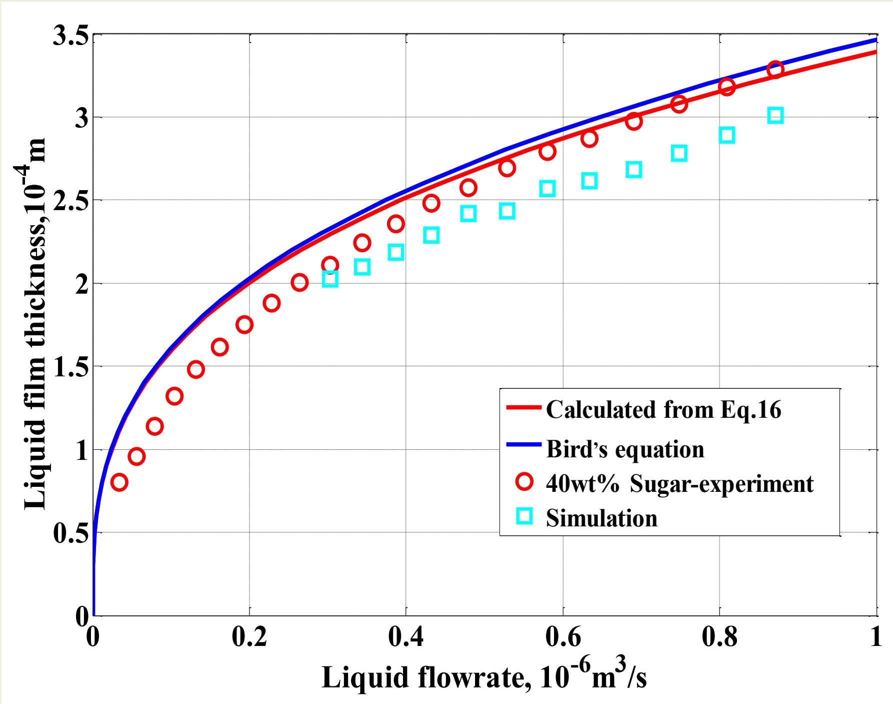

Figure 7c. The liquid film thickness comparison results of 40 wt% Sugar.

Figure 7. Calculated liquid film thickness by Eq.16 and Bird's equation compared with experiment measurements and simulation result.

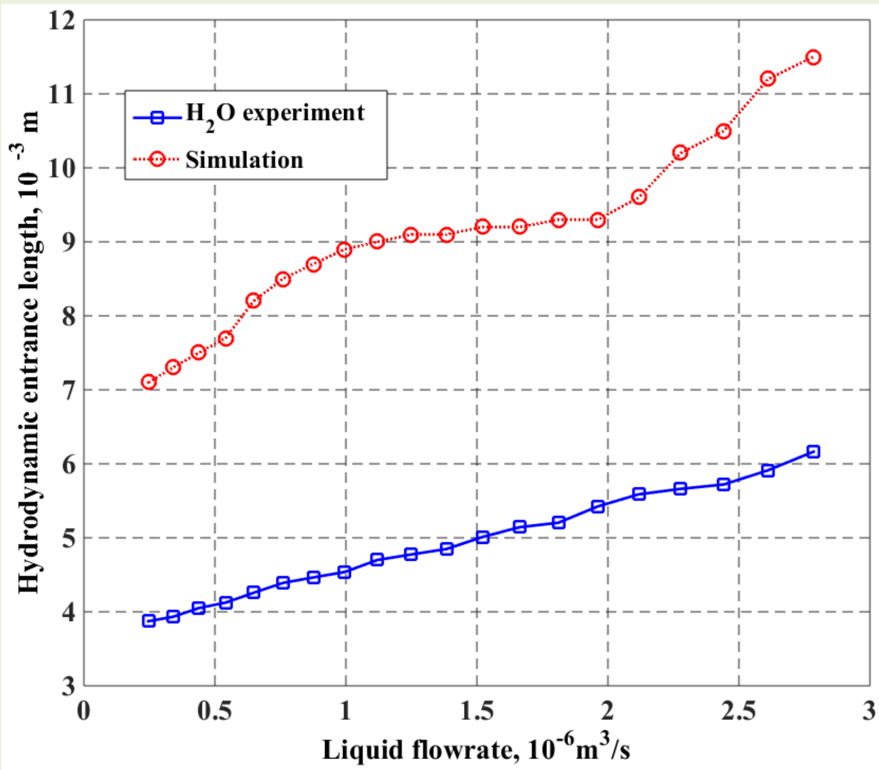

Figure 8a. The hydrodynamic entrance length comparison results of H_2O.

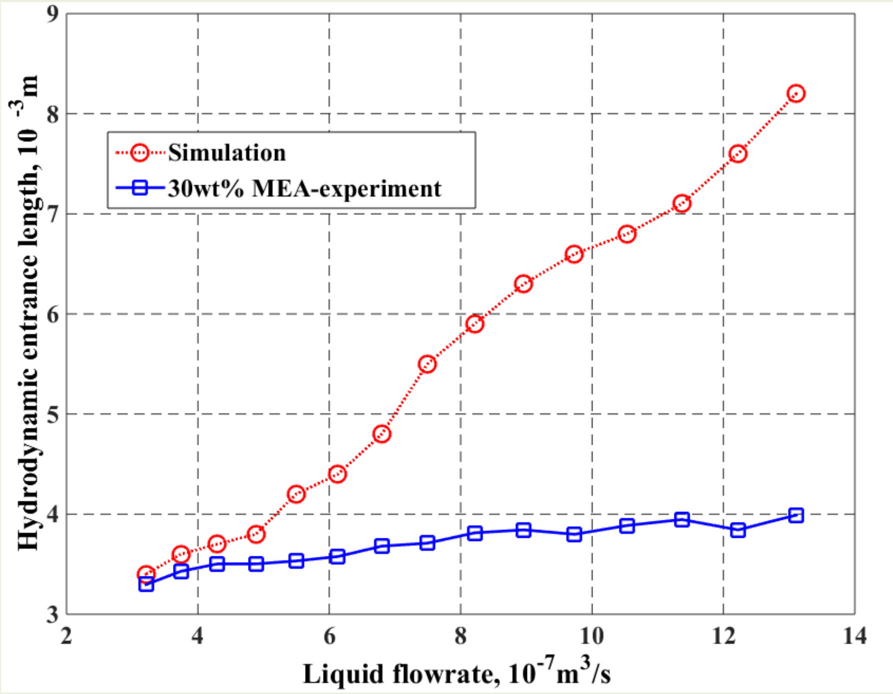

Figure 8b. The hydrodynamic entrance length comparison results of 30wt% MEA.

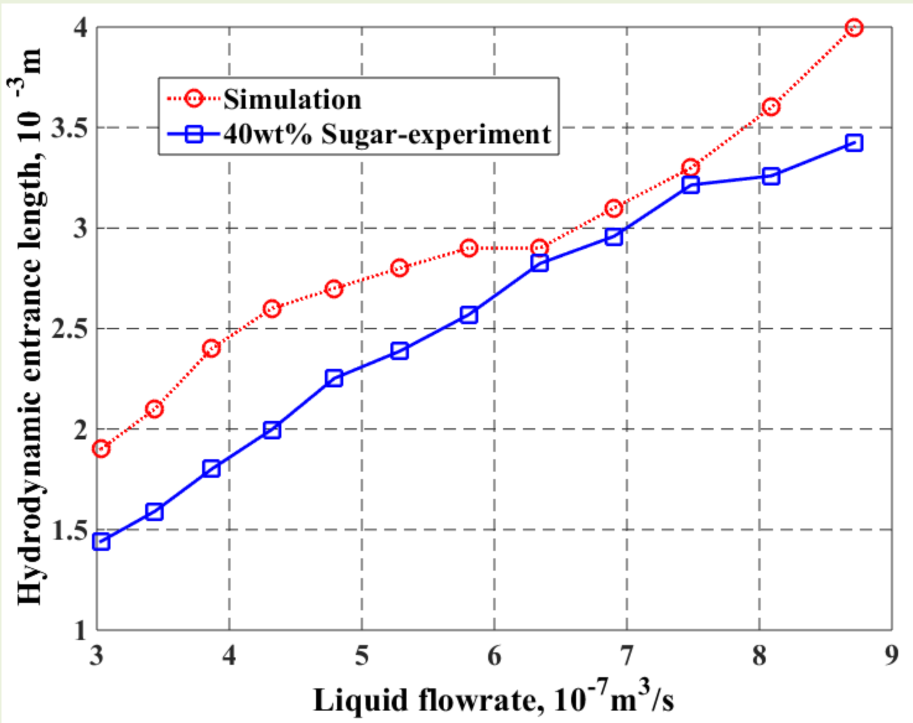

Figure 8c. The hydrodynamic entrance length comparison results of 40 wt% Sugar

Figure 8. Comparison of Hydrodynamic entrance length between experiments and simulation results.

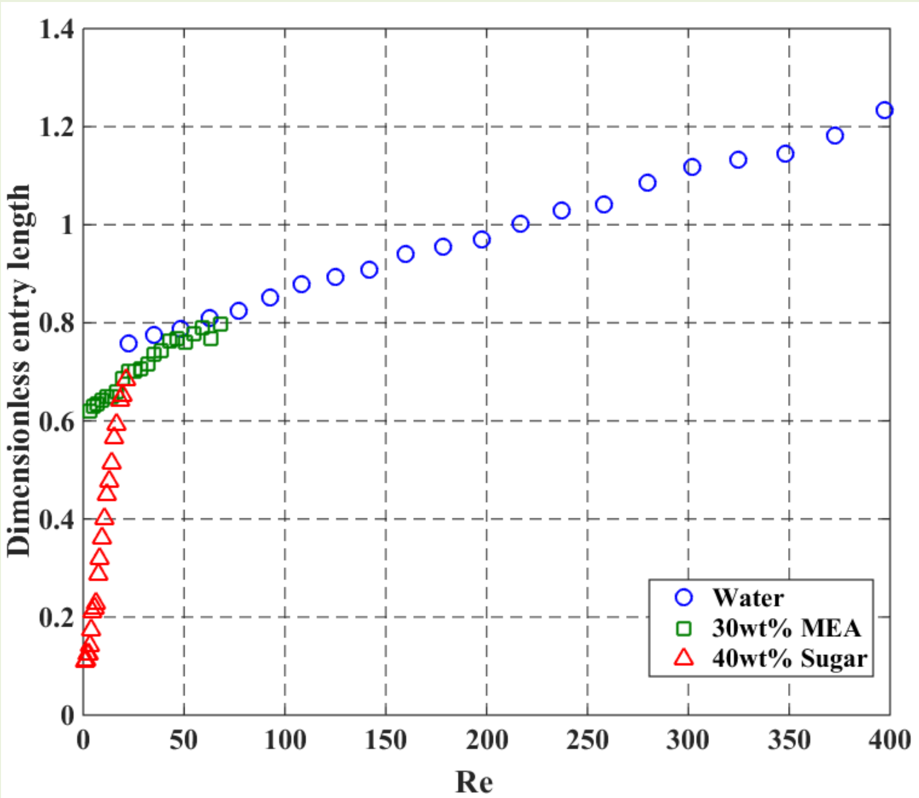

Figure 9. The relationship between the experimental hydrodynamic entrance length and the Reynolds number.

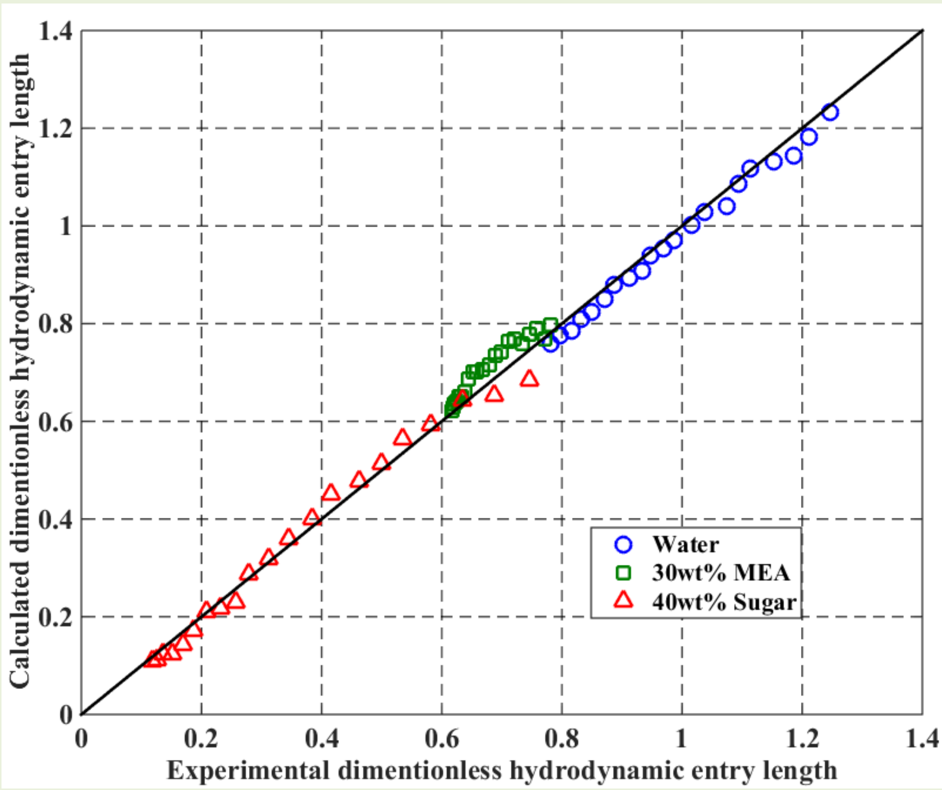

Figure 10. Crossplot between calculated and experimental hydrodynamic entrance length.

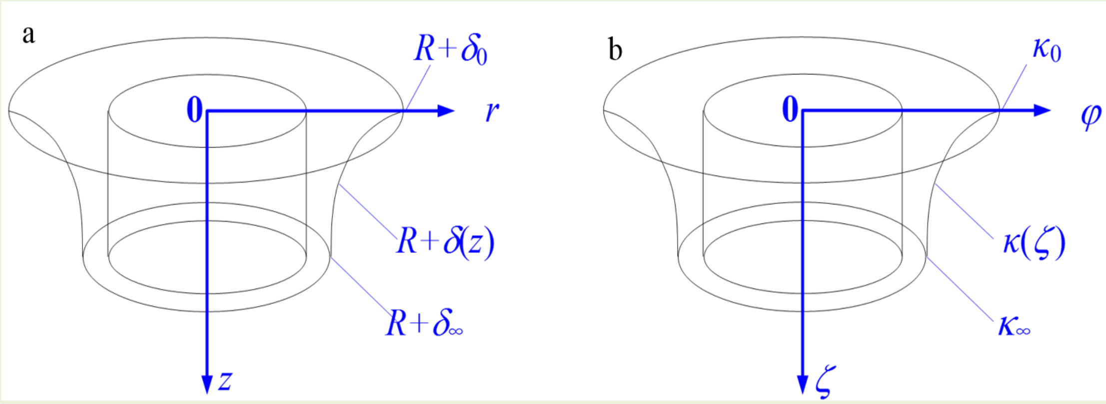

Figure 11. The schematic diagram of liquid film surface in the entrance region with normal and dimensionless coordinates.

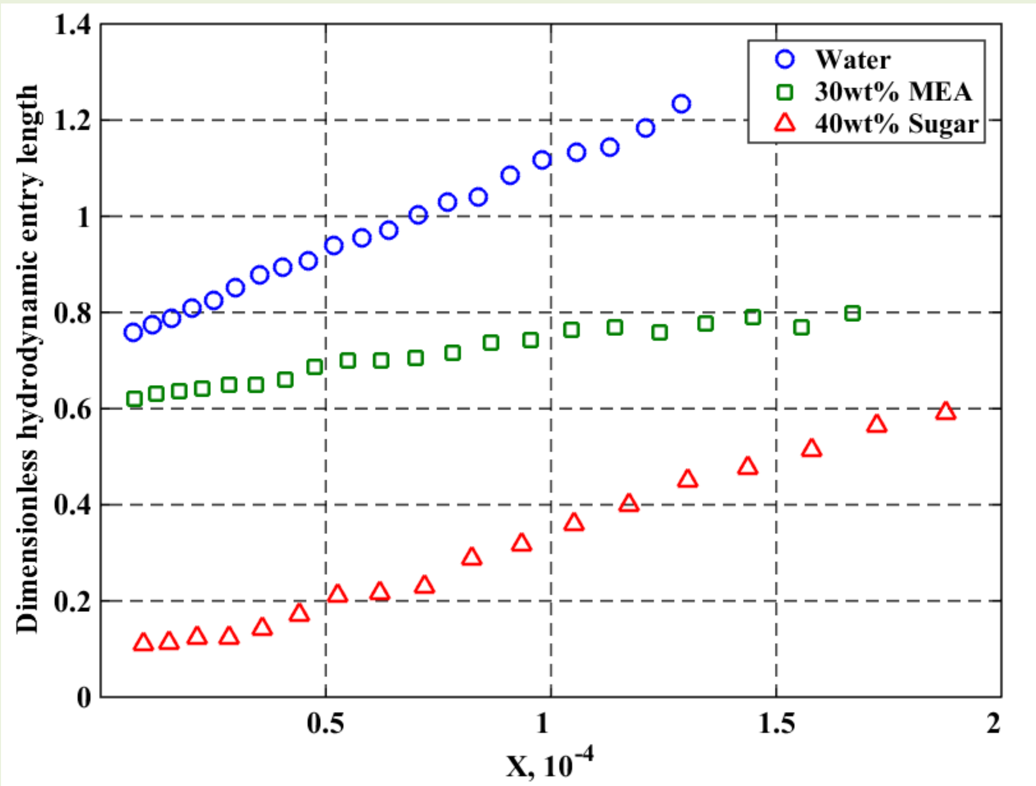

Figure 12. The experimental dimensionless hydrodynamic entry length varied with Q.

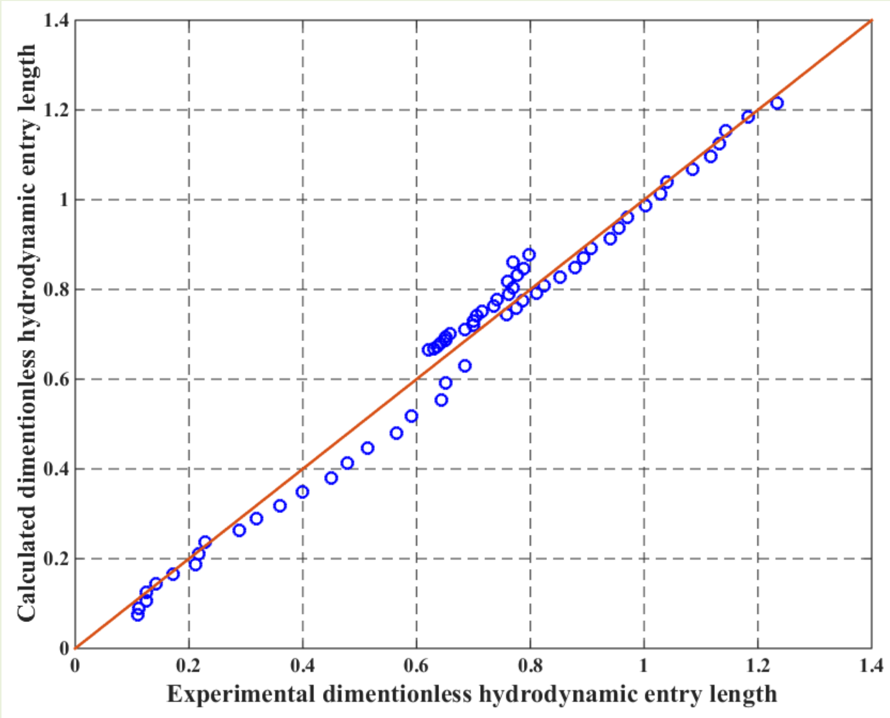

Figure 13. The parity plot of experimental and calculated dimensionless hydrodynamic entrance length.

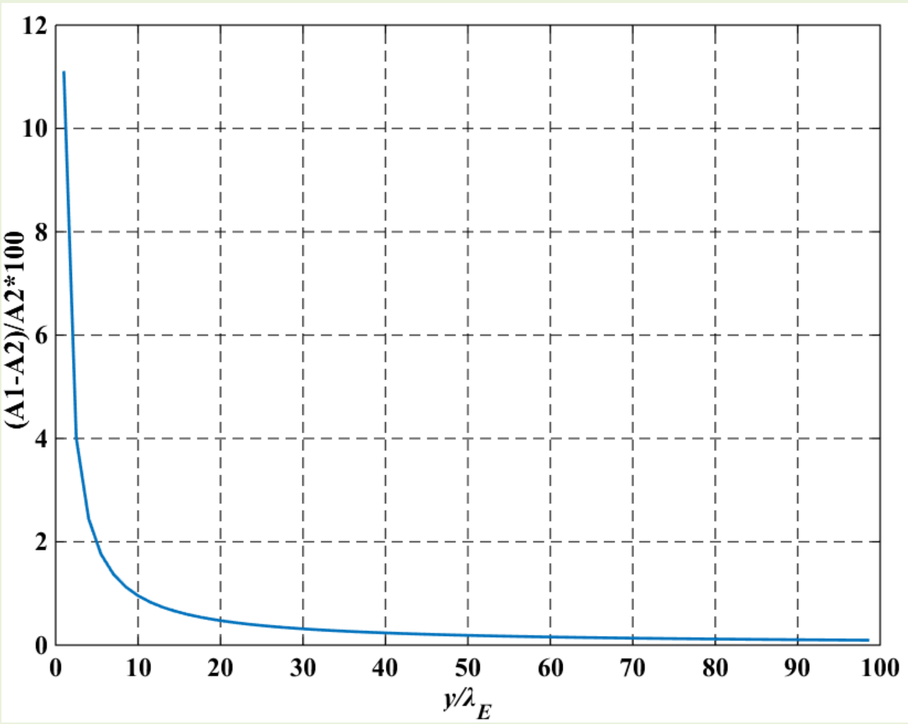

Figure 14. Relationship between (A_1-A_2)/A_2 and y/λ_E.

Tables

Table 1. Properties of working fluids at 298.15 K and a pressure of 101.325 kPa

Working fluid	ρ ($kg \cdot m^{-3}$)	μ ($mPa \cdot s$)	σ ($mN \cdot m^{-1}$)
distilled water	997.057[3]	0.8899[3]	72.01[4]
40wt% sugar solution[6]	1177.0	6.162	74.90
30wt% MEA solution	1010.6[5]	2.48[5]	60.41[4]

Table 2. The results of meshes number independent test

Meshes No.	δ (mm)	λ_E (mm)
44890	0.2057	7.6
635110	0.2062	7.7
1796700	0.2066	7.7

Table 3. Important information used for the simulations.

Settings	Choice
Simulation type	2D, unsteady
Solver	Pressure based and implicit
Multiphase model	VOF and implicit
Viscous model	Laminar
Materials	Water & air, MEA (30wt%) & air, Sugar (40wt%) & air
Operating conditions	Standard pressure, gravity
Boundary conditions	Velocity inlet, outflow
Solution controls	PISO, second order upwind

Table 4. Film thickness and hydrodynamic entrance length of distilled water

No.	Re	δ (mm)	λ_E (mm)
1	22.3779	0.1161	3.7935
2	35.1278	0.1366	3.8730
3	48.5086	0.1547	3.9322
4	62.5205	0.1675	4.0504
5	77.1634	0.1802	4.1243
6	92.4373	0.1926	4.2574
7	108.3422	0.2006	4.3904
8	124.8781	0.2127	4.4643
9	142.0451	0.2219	4.5383
10	159.8430	0.2278	4.7009
11	178.2720	0.2360	4.7748
12	197.3320	0.2426	4.8487
13	217.0230	0.2524	5.0113
14	237.3450	0.2587	5.1443
15	258.2980	0.2698	5.2035
16	279.8820	0.2750	5.4252
17	302.0971	0.2801	5.5878
18	324.9431	0.2901	5.6617
19	348.4202	0.2979	5.7209
20	372.5283	0.3034	5.9130
21	397.2674	0.3111	6.1643

Table 5. Film thickness and hydrodynamic entrance length of 40 wt% Sugar

No.	Re	δ (mm)	λ_E (mm)
1	0.8417	0.0799	0.5471
2	1.3545	0.0959	0.5621
3	1.9205	0.1139	0.6222
4	2.5396	0.1317	0.6222
5	3.2119	0.1482	0.7124
6	3.9373	0.1618	0.8627
7	4.7159	0.1749	1.0581
8	5.5477	0.1881	1.0882
9	6.4325	0.2006	1.1432
10	7.3706	0.2109	1.4409
11	8.3618	0.2241	1.5912
12	9.4061	0.2355	1.8016
13	10.5036	0.2479	1.9970
14	11.6542	0.2573	2.2525
15	12.8580	0.2695	2.3878
16	14.1149	0.2790	2.5681
17	15.4250	0.2872	2.8236
18	16.7882	0.2972	2.9589
19	18.2046	0.3079	3.2144
20	19.6741	0.3179	3.2595
21	21.1968	0.3285	3.4248

Table 6. Film thickness and hydrodynamic entrance length of 30 wt% MEA

No.	Re	δ (mm)	λ_E (mm)
1	3.0909	0.0960	3.1038
2	4.9991	0.1125	3.1481
3	7.0482	0.1263	3.1777
4	9.2380	0.1435	3.2073
5	11.5686	0.1562	3.2516
6	14.0400	0.1718	3.2516
7	16.6522	0.1846	3.2959
8	19.4052	0.1952	3.4290
9	22.2989	0.2105	3.5029
10	25.3334	0.2223	3.5029
11	28.5088	0.2376	3.5324
12	31.8249	0.2529	3.5768
13	35.2818	0.2625	3.6802
14	38.8794	0.2739	3.7098
15	42.6179	0.2852	3.8132
16	46.4971	0.2954	3.8428
17	50.5172	0.3060	3.7985
18	54.6780	0.3161	3.8871
19	58.9796	0.3255	3.9463
20	63.4220	0.3346	3.8428
21	68.0051	0.3418	3.9906

Table 7. The ratio of shear stress and gravity X and the correction factor γ in Eq.32

	X			γ		
No.	Distilled water	30 wt% MEA	40 wt% Sugar	Distilled water	30 wt% MEA	40 wt% Sugar
1	7.2687E-06	7.5895E-06	7.9080E-06	1.2757	1.0445	0.1848
2	1.1408E-05	1.2275E-05	1.2727E-05	1.3129	1.0687	0.1917
3	1.5754E-05	1.7307E-05	1.8044E-05	1.3418	1.0867	0.2139
4	2.0309E-05	2.2684E-05	2.3862E-05	1.3902	1.1039	0.2155
5	2.5063E-05	2.8406E-05	3.01781E-05	1.4232	1.1259	0.2484
6	3.0026E-05	3.4475E-05	3.6994E-05	1.4764	1.1323	0.3028
7	3.5193E-05	4.0883E-05	4.4310E-05	1.5296	1.1539	0.3737
8	4.0563E-05	4.7648E-05	5.2124E-05	1.5624	1.2066	0.3866
9	4.6137E-05	5.4757E-05	6.0438E-05	1.5951	1.2388	0.4086
10	5.1897E-05	6.2210E-05	6.9260E-05	1.6592	1.24483	0.5181
11	5.7921E-05	7.0007E-05	7.8560E-05	1.6922	1.2611	0.5753
12	6.4083E-05	7.8148E-05	8.8386E-05	1.7252	1.2831	0.6553
13	7.0478E-05	8.6633E-05	9.8691E-05	1.7896	1.3260	0.7303
14	7.7104E-05	9.5462E-05	1.0950E-04	1.8441	1.3429	0.8281
15	8.3915E-05	1.0465E-04	1.2081E-04	1.8722	1.3863	0.8830
16	9.0912E-05	1.1418E-04	1.3262E-04	1.9592	1.4034	0.9548
17	9.8141E-05	1.2404E-04	1.4492E-04	2.0253	1.3930	1.05569
18	1.0555E-04	1.3428E-04	1.5774E-04	2.0594	1.4318	1.1122
19	1.1315E-04	1.4486E-04	1.7104E-04	2.0882	1.4598	1.2146
20	1.2098E-04	1.5568E-04	1.8486E-04	2.1658	1.4277	1.2383
21	1.2905E-04	1.6702E-04	1.9917E-04	2.2656	1.4890	1.3084

Table 8. Bond number (Bo), and the parameters *m* and *n* of working fluids

Working fluids	Bo	*m*	*n*
distilled water	0.2610	5364.4685	0.0848
30wt% MEA solution	0.2944	7864.1437	1.2319
40wt% sugar solution	0.2437	2798.6857	1.0535